scientific reports

OPEN

Cobalt, nickel and zinc spinel ferrites with high transmittance and UV-blocking for advanced optical applications

Mai M. El-Masry[1]✉ & M. M. Arman[2]

This study successfully synthesized and characterized $CoFe_2O_4$, $NiFe_2O_4$, and $ZnFe_2O_4$ ferrite nanoparticles. The results showed that $CoFe_2O_4$ and $NiFe_2O_4$ exhibited ferrimagnetic behavior, while $ZnFe_2O_4$ demonstrated antiferromagnetic properties. These magnetic characteristics influence the material's response to electromagnetic radiation, such as visible and infrared light. Optical studies revealed that $CoFe_2O_4$ had the highest radiation absorption, while $ZnFe_2O_4$ showed superior reflection and transmission. The ferrites' band gap energies, ranging from 3.3 to 3.6 eV, played a key role in their optical properties, with higher energy absorption and lower energy reflection. The refractive index varied with photon energy, reaching its peak at lower energy levels due to oxygen vacancies. Additionally, the optical conductivity increased with higher photon energy, peaking at 4.3 eV. These findings suggest promising applications in light transmission and sensing, with ferrites offering versatile optical properties that can be tailored for various uses.

In this article, there are three different spinel ferrites, Co ferrite, Ni ferrite and Zn ferrite nano particles. Spinel ferrites (AB_2O_4) are a class of inorganic compounds. They are composed of divalent metal cations, A, and tetravalent metal cations, B, which are octahedrally coordinated and share oxygen ions to create a cubic close-packed structure. The physical and magnetic properties of these materials make them useful in various applications[1,2].

The spinel ferrite has the same general mineral spinel crystal structure, in which iron (II) oxide, Fe_3O_4, serves as the prototype. In the spinel structure, each oxygen ion is shared by four metal cations, two of type A and two of type B. The metal cations are octahedrally coordinated, meaning that each cation is surrounded by six oxygen ions. Oxygen ions are arranged in a cubic close-packed structure, in which each oxygen ion is coordinated to eight metal cations. The spinel ferrites can be seen as a special case of the general ABX_3 structure, in which the X site is occupied by oxygen and the A and B sites are alternately occupied by divalent and tetravalent metal cations[3–5].

The magnetic properties of AB_2O_4 are determined by the cations on the A and B sites. If the A and B cations have the same magnetic moment, the material is non-magnetic. If the cations distributed in the A and B sites possess different magnetic moments, the material is magnetic. The magnetic moment of the spinel ferrites is calculated by the coupling between the A and B cations[4,6,7].

Spinels ferrites, particularly those based on cobalt (Co), nickel (Ni), and zinc (Zn), have garnered significant attention due to their unique optical properties and potential applications in advanced optical devices. These materials exhibit high transmittance in the visible spectrum while effectively blocking ultraviolet (UV) radiation, making them ideal candidates for UV shielding, smart windows, and optoelectronic devices. The choice of this specific composition cobalt, nickel, and zinc spinel ferrites is driven by their tunable electronic structure, which arises from the synergistic effects of transition metal ions occupying tetrahedral and octahedral sites within the spinel lattice. This structural arrangement influences their bandgap energy, magnetic properties, and optical absorption characteristics, as highlighted in recent studies[8,9]. For instance, cobalt ferrites are known for their excellent magnetic properties and moderate optical transparency, while nickel ferrites offer enhanced stability

[1]Basic Science Dept., Higher Engineering Institute, Thebes Academy, Cairo, Egypt. [2]Materials Science Lab (1), Physics Department, Faculty of Science, Cairo University, Giza, Egypt. ✉email: mai.elmasry@thebes.edu.eg; mai_elmasry@hotmail.com

and tunable UV-blocking capabilities[10]. Zinc ferrites contribute to improved transparency and reduced optical losses, as demonstrated in diamond-like carbon coatings and thin films[11]. Furthermore, the incorporation of these elements into a single-phase spinel structure allows for the optimization of both optical and magnetic functionalities, as evidenced by recent advancements in ceramic processing and material synthesis techniques[12]. By leveraging these advantages, the present study aims to systematically investigate the structural, optical, and functional properties of cobalt, nickel, and zinc spinel ferrites to pave the way for their integration into cutting-edge optical technologies.

In antiferromagnetic materials like $ZnFe_2O_4$, the magnetic moments tend to align in opposite directions, leading to a cancelation of the overall magnetic moment. This magnetic behavior can influence the absorption properties differently compared to ferrimagnetic materials. The magnetic ordering in ferrites can influence their electronic band structure. Changes in the band gap energy, as observed in ferrites, can affect the absorption and transmission of light. Variations in the band structure can lead to different energy levels and transitions, impacting the optical properties of the material.

Magnetic behavior is inherently linked to the spin of electrons. Spin-dependent processes, such as spin-dependent transitions and spin-flip scattering, can occur in magnetic materials. These processes can contribute to changes in the absorption and transmission properties of light, particularly in the presence of an external magnetic field. Magnetic behavior may introduce optical anisotropy in ferrites, meaning that the optical properties may vary with the direction of light propagation concerning the crystallographic axes. This anisotropy can lead to directional dependence in absorption and transmission properties.

Recent studies underscore the growing significance of spinel ferrites in optical technologies, leveraging their unique magnetic, electronic, and structural properties. The article[13] highlights advancements in synthesis techniques for spinel ferrites, emphasizing their tunable bandgaps and absorption characteristics for photonic devices. Algarni et al. explores structural optimization of these materials, demonstrating enhanced light-matter interactions through controlled crystallite size and doping, critical for optoelectronic sensors[12]. Researchers elucidate the role of cation distribution and defects in modulating optical behavior, linking these features to applications in UV–Vis-NIR spectroscopy[11]. Researchers investigate nanocomposite spinel ferrites, revealing their potential in magneto-optical data storage and plasmonic systems[10]. A study in[9] integrates spinel ferrites with diamond substrates, achieving robust optical coatings with high thermal stability for harsh-environment sensors. The interplay between magnetic ordering and optical responses was examined, advancing their use in spintronic-photonic hybrid devices[8].

$CoFe_2O_4$, $NiFe_2O_4$, and $ZnFe_2O_4$ ferrite nanoparticles were investigated recently for their promising magnetic and optical properties. The ferrimagnetic behavior of $CoFe_2O_4$, coupled with its optical properties, can be utilized in magneto-optical devices. These devices exploit the interaction between magnetic and optical phenomena for applications like magneto-optical sensors and data storage[14–16]. A comparison between different properties of $CoFe_2O_4$, $NiFe_2O_4$, and $ZnFe_2O_4$ ferrite nanoparticles based on published work are listed in Table 1

$NiFe_2O_4$'s magnetic and optical properties can be harnessed in magneto-optical modulators, where an external magnetic field modulates the intensity of light[36,37]. This can be useful in optical communication and signal processing. The magnetic behavior of $NiFe_2O_4$ nanoparticles, coupled with their optical properties, makes them suiTable for sensing applications. They can be utilized in magnetic field sensors or as components in optically based sensors for various environmental parameters[38,39].

$ZnFe_2O_4$'s antiferromagnetic behavior and reflectance properties make it suiTable for optical filters[40]. These filters can selectively transmit or reflect specific wavelengths of light, finding applications in optical communication and imaging systems. $ZnFe_2O_4$ nanoparticles can be incorporated into transparent conductive films for applications in optoelectronic devices such as touchscreens, solar cells, and light-emitting diodes (LEDs). $ZnFe_2O_4$ may find application in LEDs due to its optical properties. Incorporating these nanoparticles into the LED structure can potentially enhance its performance and efficiency[41–43].

The optical applications of $CoFe_2O_4$, $NiFe_2O_4$, and $ZnFe_2O_4$ ferrite nanoparticles span a wide range of technologies, from magneto-optical devices and sensors to photocatalysis and biomedical imaging. Their unique combination of magnetic and optical properties makes them versatile materials for advancing various fields of optics and photonics.

Property	$CoFe_2O_4$	$NiFe_2O_4$	$ZnFe_2O_4$	Ref
Band Gap (eV)	1.0–1.5	2.0–3.5	1.5–2.2	[17–21]
Color	Black	Black/Gray	Yellowish/Brownish	
optical absorption	strong absorption in the visible and near-infrared regions	relatively lower optical absorption due to its wider band gap	moderate optical absorption	[17,21–23]
Photoluminescence	Weak	Weak	Visible/NIR	[24–27]
Magnetic Ordering	Ferromagnet	Weak Ferro/Ferrimagnet	Antiferromagnet	[18,19]
Curie/Neel Temp. (°C)	~590	~580	~600	[28–30]
Magnetic Anisotropy	Cubic	Cubic/Uniaxial	-	[31–33]
Response to External Stimuli	sensitive to temperature, pressure, and magnetic fields,	high stability and resistance to oxidation	sensitive to light, temperature, and pressure	[29,32–35]
Applications	photocatalysis and solar energy conversion	optoelectronic devices and transparent coatings	sensors, pigments, and photocatalysis	[18,19]

Table 1. A comparison between different properties of $CoFe_2O_4$, $NiFe_2O_4$, and $ZnFe_2O_4$ ferrite nanoparticles.

Experimental work
Synthesis of the nano ferrites
Cobalt nitrate, nickel nitrate, zinc nitrate, and iron nitrate, each with a purity of 99.9%, were bought from Sigma-Aldrich. The samples were synthesized by employing the citrate combustion method[44]. The stoichiometric blend of metal nitrates and citric acid, soluble in deionized water, was prepared with a citrate-to-nitrates ratio of 1:1. To achieve a neutral pH of 7, NH_4OH solution was used for a pH change. The resulting solution underwent heating on a hot plate until ash formation occurred.

Nanoferrites characterizations and analysis
The XRD technique was used to study the phase identification and determining the crystallite size via Bruker advance D8 diffractometer with a wavelength $\lambda = 0.15418$ mm. The diffraction peaks were indexed with the ICDD cards 22–1086, 44–1485 and 22–1012. FESEM was used to study the surface morphology of the samples was studied using FESEM Model Quanta 250 FEG. The function groups of the samples were studied using Fourier-transformed infrared (FTIR) which was scanned via a FTIR spectrometer (Nicolet iS10, USA, 1 cm^{-1} spectral resolution). The BET (Brunauer, Emmett, and Teller) surface area of the samples was studied using the BET, NLDFT Ads. model. The surface chemistry and electronic structure of the samples were studied using X-ray photoelectron spectroscopy (XPS, K-ALPHA, Thermo Fisher Scientific, USA). Cary 5000 UV–Vis–NIR Spectrophotometer ($\lambda = 200$–2000 nm, Version 1.12, double beam mode) was used to study the optical analysis of the samples. the magnetic properties of the ferrite were performed using the vibrating sample magnetometer (VSM; 9600–1 LDJ, USA).

Results and discussion
XRD
Figure 1 shows the XRD pattern of the nano ferrite samples AFe_2O_4 (A: Co, Ni and Zn). The XRD data were indexed with the ICDD cards 22-1086, 44-1485 and 22-1012 for the $CoFe_2O_4$, $NiFe_2O_4$, and $ZnFe_2O_4$, respectively[45]. All samples crystallized in a single-phase cubic spinel structure (space group Fd-3 m) with no detectable impurities, confirming the phase purity of the synthesized ferrites. The sharp and well-defined diffraction peaks align with recent studies highlighting the importance of controlled synthesis conditions in achieving structurally ordered spinel ferrites[46]. the values of lattice parameter (a) for the samples were calculated on the bases on the cubic structure using the following equation[46,47].

$$\frac{1}{d^2} = (h^2 + k^2 + l^2)\frac{1}{a^2} \tag{1}$$

where d denotes the d-spacing and (hkl) are the miller indices The unit cell volume (V) was derived from

$$V = a^3, \tag{2}$$

with values tabulated in Table 2). Notably, the lattice parameters and peak broadening trends correlate with cation distribution and crystallite size effects, as discussed in recent works on analogous spinel systems[48,49].

The theoretical density (D_x) of the samples was calculated using equation[46,49] (3).

$$Dx = \frac{ZM}{N_A V} \tag{3}$$
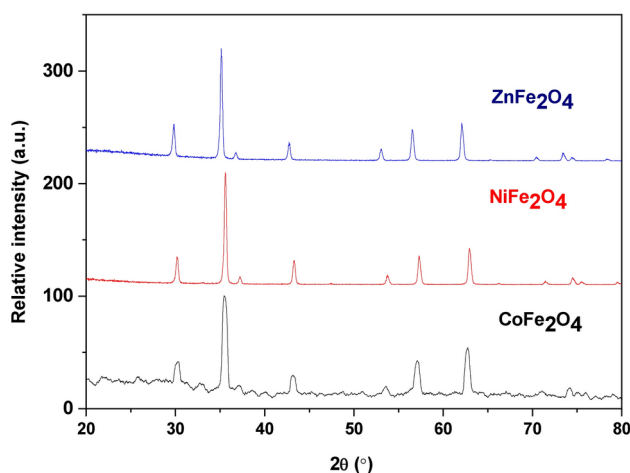
Fig. 1. XRD Patterns of Nano Ferrite Samples. XRD patterns of $CoFe_2O_4$, $NiFe_2O_4$, and $ZnFe_2O_4$ nanoparticles, indexed with ICDD cards 22–1086, 44–1485, and 22–1012, confirming a single-phase cubic spinel structure. The calculated lattice parameters, unit cell volumes, and crystallite sizes validate the nano-scale dimensions of the samples.

Samples	a(Å)	V(Å³)	D_x (g/cm³)	L (nm) (XRD)
$CoFe_2O_4$	8.368	585.92	5.318	71.50
$NiFe_2O_4$	8.357	583.75	5.337	28.28
$ZnFe_2O_4$	8.426	598.22	5.324	30.26

Table 2. The lattice parameter (a), the unit cell volume (V), the theoretical density (D_x) and the average crystalline size (L) for the samples.
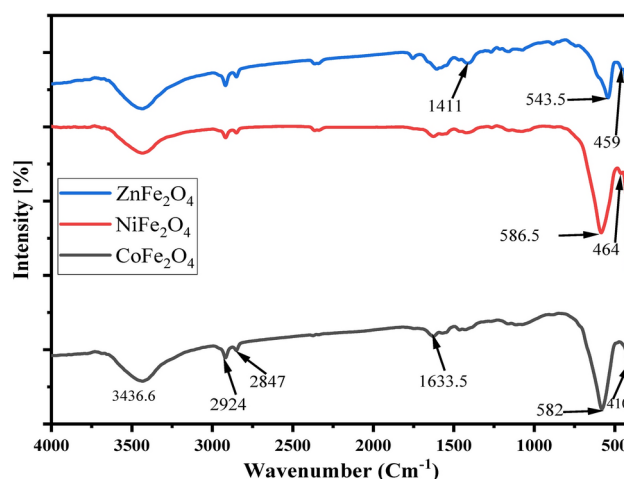
Fig. 2. FTIR Spectra of Ferrite Samples. FTIR spectra of $CoFe_2O_4$, $NiFe_2O_4$, and $ZnFe_2O_4$ nanoparticles showing characteristic vibrational modes. Peaks include Fe–O and Co–O stretching ($CoFe_2O_4$), Ni–O and Fe–O modes ($NiFe_2O_4$), and Zn–O and Fe–O stretching ($ZnFe_2O_4$). Additional peaks represent functional groups such as C–H and C=O vibrations, indicative of the materials' chemical composition and structural characteristics.

where Z = 8, M denotes the molecular weight, N_A is the Avogadro's number and V denotes the unit cell volume. Further validating the structural consistency of the synthesized ferrites. These findings are consistent with literature reports emphasizing the role of cation substitution (Co, Ni, Zn) in modulating spinel lattice dimensions while retaining structural integrity, a critical factor for optical and functional performance in advanced applications.

The Scherer equation[50,51] was used to calculate the average crystallite size (L) of the spinel ferrites.

$$L = \frac{0.9\lambda}{\beta cos\theta} \qquad (4)$$

where λ refers the XRD wavelength, β denotes the full width at half maximum intensity and θ is the Bragg angle. The values of L are reported in Table 2 and confirm the prepared samples have nano dimensions[52].

FTIR

FTIR spectroscopy is a powerful tool for the characterization of inorganic materials like cobalt ferrite. This technique can provide information on the functional groups present in a sample, as well as the relative abundance of those groups. The infrared spectrum of nanoparticles is a valuable tool for understanding the structure and composition of this material. This information is important for optimizing the properties. Figure 2 illustrates the FTIR spectra of $CoFe_2O_4$, $NiFe_2O_4$ and $ZnFe_2O_4$.

The infrared spectrum of cobalt ferrite nanoparticles is dominated by Fe–O and Co–O stretching vibrations, with some contribution from bending vibrations of the same groups. The symmetric and asymmetric stretching of the Fe–O bonds are well resolved, while the Co–O stretching mode is significantly broader.

The presence of these functional groups indicates that the cobalt ferrite nanoparticles are primarily made up of Co-Fe–O octahedra. This confirms what was previously predicted by X-ray diffraction studies of this material. The FTIR spectrum also provides quantitative information on the amount of each type of atom in the cobalt ferrite nanoparticles. From the relative intensities of the various stretching and bending vibrations, it is estimated that the cobalt ferrite nanoparticles contain approximately equal amounts of Fe and Co. The 3436 cm⁻¹ peak is assigned to the C-H stretching vibration of aromatic species. The 2924 cm⁻¹ peak is assigned to the alkene C-H stretching vibrational mode of olefins[53]. The 2847 cm⁻¹ peak is attributed to the C-H bending region[54]. The 1633 cm⁻¹ peak is attributed to the C=O stretching mode of carbonyl compounds. The 1411cm⁻¹ peak in an FTIR spectrum is typically attributed to asymmetric stretching of carbon–carbon single bonds (stretching of C–C
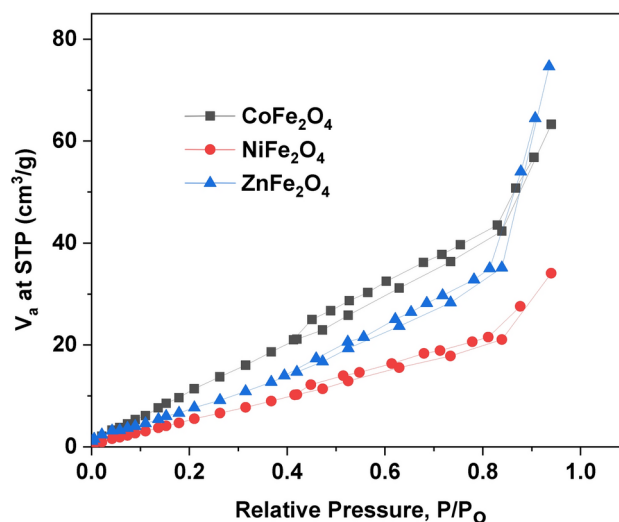
Fig. 3. BET surface area of (CoFe$_2$O$_4$, NiFe$_2$O$_4$, and ZnFe$_2$O$_4$) samples.

Samples	Specific surface area (m²/g)	Total pore volume (cm³/g)	Average pore diameter (nm)
CoFe$_2$O$_4$	120	0.098	3.26
NiFe$_2$O$_4$	44	0.053	4.72
ZnFe$_2$O$_4$	49	0.116	9.42

Table 3. The total pore volume, specific surface area, and average pore diameter of CoFe$_2$O$_4$, NiFe$_2$O$_4$, and ZnFe$_2$O$_4$ ferrites.

or C=C bonds). The 824 cm^{-1} peak is attributed to the C-N stretching vibration. Finally, the 582 cm^{-1} peak is assigned to the stretching vibration of the Fe–O–Fe bonded group, while the peak seen at 410 cm^{-1} is attributed to the stretching vibration of Fe–O bonds or iron oxyhydroxides and is known as the quaternary ferrite peak. It is a characteristic peak of the ferrite material, representing the mixed ferric-oxygen environment that is formed in the film[55–58].

The FTIR spectrum of nickel ferrite was studied. The spectrum showed that the peak at 586 cm^{-1} corresponds to the Ni–O stretching mode, while the peak at 464 cm^{-1} corresponds to the Fe–O stretching mode. The results indicate that nickel ferrite has a symmetric structure, which agrees with previous studies.

The zinc ferrite FTIR spectrum was measured. A strong peak at 543 cm^{-1} refers to the Zinc-Oxygen (Zn–O) bond stretching frequency. A second peak at 459 cm^{-1} refers to the Ferric-Oxygen (Fe–O) bond stretching frequency. These peaks are expected for a zinc ferrite material, indicating the presence of both zinc and ferric oxide in the sample[55,56].

BET

Figure 3 shows the adsorption–desorption isotherm of CoFe$_2$O$_4$, NiFe$_2$O$_4$, and ZnFe$_2$O$_4$ nanoparticles. The BET isotherms of the samples are type II and H3 hysteresis loop according to IUPAC classifications[59,60]. Table 3 contains the values of total pore volume, specific surface area, and average pore diameter of the investigated ferrite samples[61,62].

FESEM

The morphology of AFe$_2$O$_4$ (A: Co, Ni and Zn) was studied using FESEM. The FESEM images confirm the presence of spherical nanoparticle clusters for CoFe$_2$O$_4$ and ZnFe$_2$O$_4$, while NiFe$_2$O$_4$ exhibits a unique cotton-like morphology, as shown in Fig. 4. These observations align with previous studies on spinel ferrites, where similar morphologies were reported to influence optical and magnetic properties[63,64]. The grain size of the CoFe$_2$O$_4$ and ZnFe$_2$O$_4$ range in 50–90 nm which assures that AFe$_2$O$_4$ (A: Co, Ni and Zn) were prepared in nano scale. Notably, the porous nature of the surfaces, as observed in the FESEM images, plays a critical role in enhancing the material's functionality. Porous structures provide a higher surface-to-volume ratio, enabling increased interaction with incident light[63,65,66]. Porous structures provide a higher surface area, allowing for more interaction with incident light[66–68]. This characteristic is particularly advantageous for applications such as sensors, heavy metal removal, and optical filters, where enhanced light-matter interactions are desired[68]. Furthermore, the integration of porous ferrites into light-emitting devices can significantly improve their efficiency, making them suitable for advanced technologies like light-emitting diodes (LEDs) and laser systems.
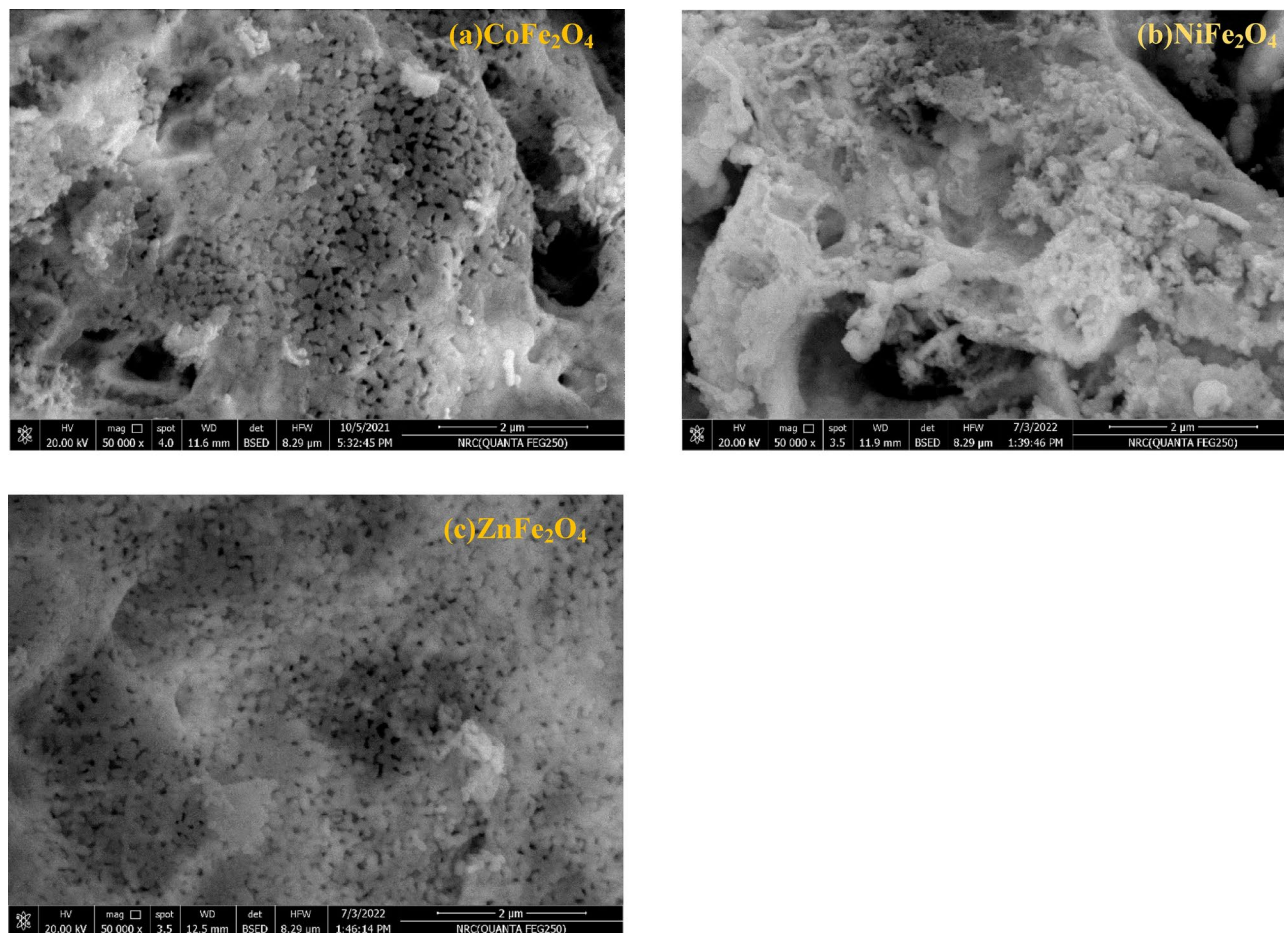
Fig. 4. FESEM Images of Ferrite Morphology. FESEM images showing the morphology of $CoFe_2O_4$, $NiFe_2O_4$, and $ZnFe_2O_4$ nanoparticles. $CoFe_2O_4$ and $ZnFe_2O_4$ exhibit spherical clusters, while $NiFe_2O_4$ displays a cotton-like morphology. All samples confirm a porous structure with particle sizes in the nano range of 50–90 nm.

X- ray photoelectron spectroscopy (XPS):

X-ray photoelectron spectroscopy (XPS) is a critical tool for elucidating the surface chemistry, electronic structure, and cation distribution in spinel ferrites such as cobalt ferrite ($CoFe_2O_4$), nickel ferrite ($NiFe_2O_4$), and zinc ferrite ($ZnFe_2O_4$). In $CoFe_2O_4$, XPS spectra typically reveal Co $2p_{3/2}$ and Co $2p_{1/2}$ peaks at 781.57 eV and 796.56 eV, respectively, with satellite peaks characteristic of Co^2_+ in octahedral coordination, as published in our previous article[69]. As shown in Fig. 5 (a, b), the XPS spectra of $NiFe_2O_4$ and $ZnFe_2O_4$ exhibit distinct features[70]. The Fe 2p region displays binding energies of $\sim$ 712 eV (Fe $2p_{3/2}$) and $\sim$ 724 eV (Fe $2p_{1/2}$), confirming the presence of Fe^3_+ in both tetrahedral and octahedral sites, while the O 1s peak near 530 eV reflects metal–oxygen bonding. For $NiFe_2O_4$, the Ni $2p_{3/2}$ and Ni $2p_{1/2}$ peaks at 855 eV and $\sim$ 873 eV, respectively, along with shake-up satellites, confirm Ni^2_+ in octahedral sites, with Fe^3_+ signatures consistent with those in $CoFe_2O_4$. In $ZnFe_2O_4$, the Zn $2p_{3/2}$ and Zn $2p_{1/2}$ peaks at $\sim$ 1021 eV and $\sim$ 1044 eV, respectively, indicate Zn^2_+ in tetrahedral sites, while the Fe^3_+ binding energies align with those in other ferrites. The O 1s spectra across all three materials consistently exhibit peaks near 530 eV, attributed to lattice oxygen. These XPS analyses provide valuable insights into cation valence states, site occupancy, and surface chemistry, which are pivotal for tailoring their magnetic, catalytic, and electronic properties for applications in spintronics, sensors, and energy storage. Table 4 highlights the cation distribution, oxidation states, and surface chemistry of both ferrites, with $ZnFe_2O_4$ showing carbon adsorption and $NiFe_2O_4$ exhibiting a cleaner surface.

Optical properties

All the spinel ferrites under investigation absorbed radiation in the UV-region, while they reflected and transmitted radiation with high intensity in visible (VIS), near infrared (NIR) and short-wave infrared regions from 400 nm to 2 μm, as shown in Fig. 6 (a–c). The variation in optical band gap, Urbach energy, and optical absorption of these ferrites are caused by lattice distortions induced by different cations because of oxidation of A-site cations. These lattice distortions result in different energy levels and band gap widths. As a result, oxygen vacancies are produced in the structure which has a significant impact on the optical properties.

The prepared AFe_2O_4 (A: Co, Ni and Zn) ferrites could be used for blocking UV radiation, NIR (800–1100 nm) radiation, and shortwave infrared radiation sensors. The high transmission in the NIR region makes the
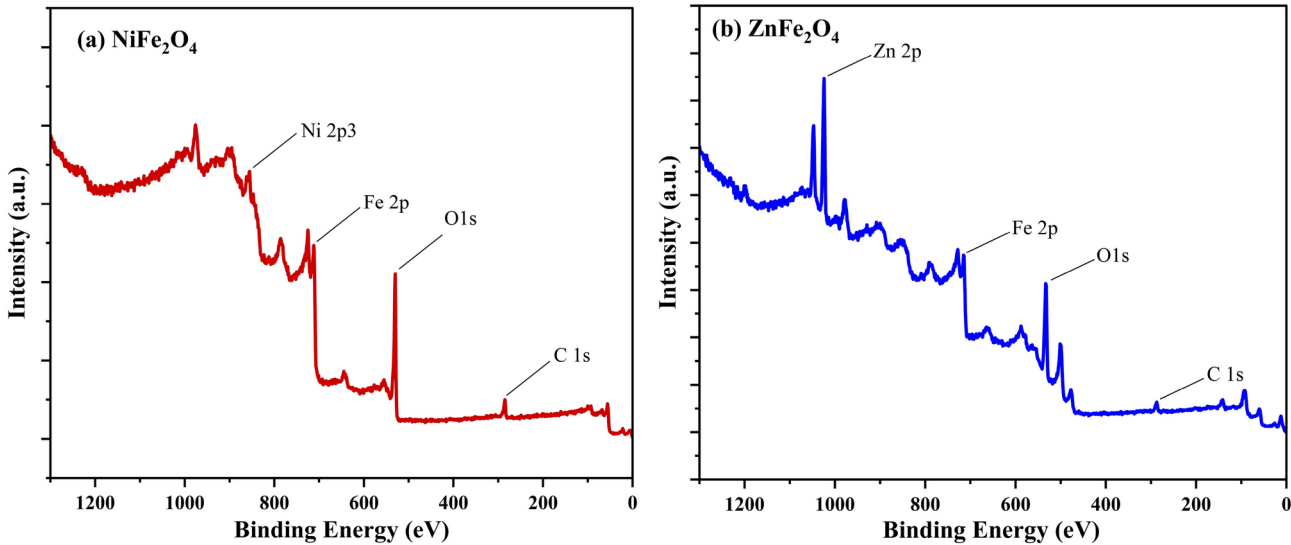
Fig. 5. XPS spectra of ($NiFe_2O_4$ and $ZnFe_2O_4$).

$ZnFe_2O_4$	Peak BE	Atomic %	$NiFe_2O_4$	Peak BE	Atomic %
Zn2p	1022.32	18.22	O1s	530.31	57.08
O1s	530.91	49.45	Fe2p	712.03	28.88
Fe2p	712.48	16.36	C1s	285.33	0
C1s	285.48	15.96	Ni2p3	855.53	14.04

Table 4. $ZnFe_2O_4$ and $NiFe_2O_4$ elemental compositions and chemical states.

samples investigated suiTable for solar energy collection. The ferrites exhibited excellent chemical stability in water, which enabled them to be used in various optical devices such as solid-state lasers, lasers, and optical fibers. The ferrites can also be used in optoelectronic components such as light-emitting diodes (LEDs) and photodetectors[71–76].

$CoFe_2O_4$ was found to be the largest absorb of radiation among the studied ferrites ranging from 190 to 2000 nm, as shown in Fig. 6 (a). In contrast, Zn Fe_2O_4 was found to be the largest reflector and transmitter of radiation in the same range as shown in Fig. 6 (a, b). This suggests that these two ferrites are suiTable for different applications depending on their optical properties. By controlling their composition and fabrication conditions, the optical properties can be tailored to meet specific requirements (Fig. 7).

Using Tauc's relation (Eq. 1) [77], we calculated the band gap energy (E_g) values of $CoFe_2O_4$, $NiFe_2O_4$, and $ZnFe_2O_4$ ferrites to be ranging from 3.3 eV to 3.6 eV (listed in Table 5). These observed E_g values are consistent with the optical properties of the examined ferrites, as they absorb radiation at high incident photon energy and reflect radiation at lower energy of the incident photon. Moreover, the E_g values we obtained are in line with those reported in the literature.

$$(\alpha h\nu)^x = B(h\nu - E_g) \tag{5}$$

where, B is a constant, ($h\nu$) is the photon energy. x depends on the type of transition for x = 2, is direct allowed band gap (**Eg$_{dir.}$**) and x = ½, (**Eg$_{ind.}$**) indirect allowed band gap.

The extrapolation of the straight line with x-axis gives the direct band gap (**Eg$_{dir.}$**) and the indirect band gap (**Eg$_{ind.}$**) as shown in Fig. 8 (a,b). The obtained enrgy gap values are listed in Table 5. From these values, it can be seen that there is only a small variation between the investigated ferrites provide further evidence that the investigated ferrites have almost the same crystal structure. The Urbach energy E_u is a measure of structural disorder in a material and is calculated from the exponential decrease of the absorption coefficient (α) of the material as a function of photon energy [78]. The Urbach energy can be calculated from α of the material over a range of photon energies. The Urbach energy E_u of the investigated samples can be calculated by fitting an exponential function to the absorption coefficient, and extracting the decay constant Fig. 8 (c). The Urbach energy provides an indication of the stability of the material, with higher Urbach energies corresponding to more sTable materials. This can be useful for the design and optimization of materials for various applications [79,80].

$$\alpha = \alpha_o e^{\frac{(h\nu - E_g)}{E_u}} \tag{6}$$
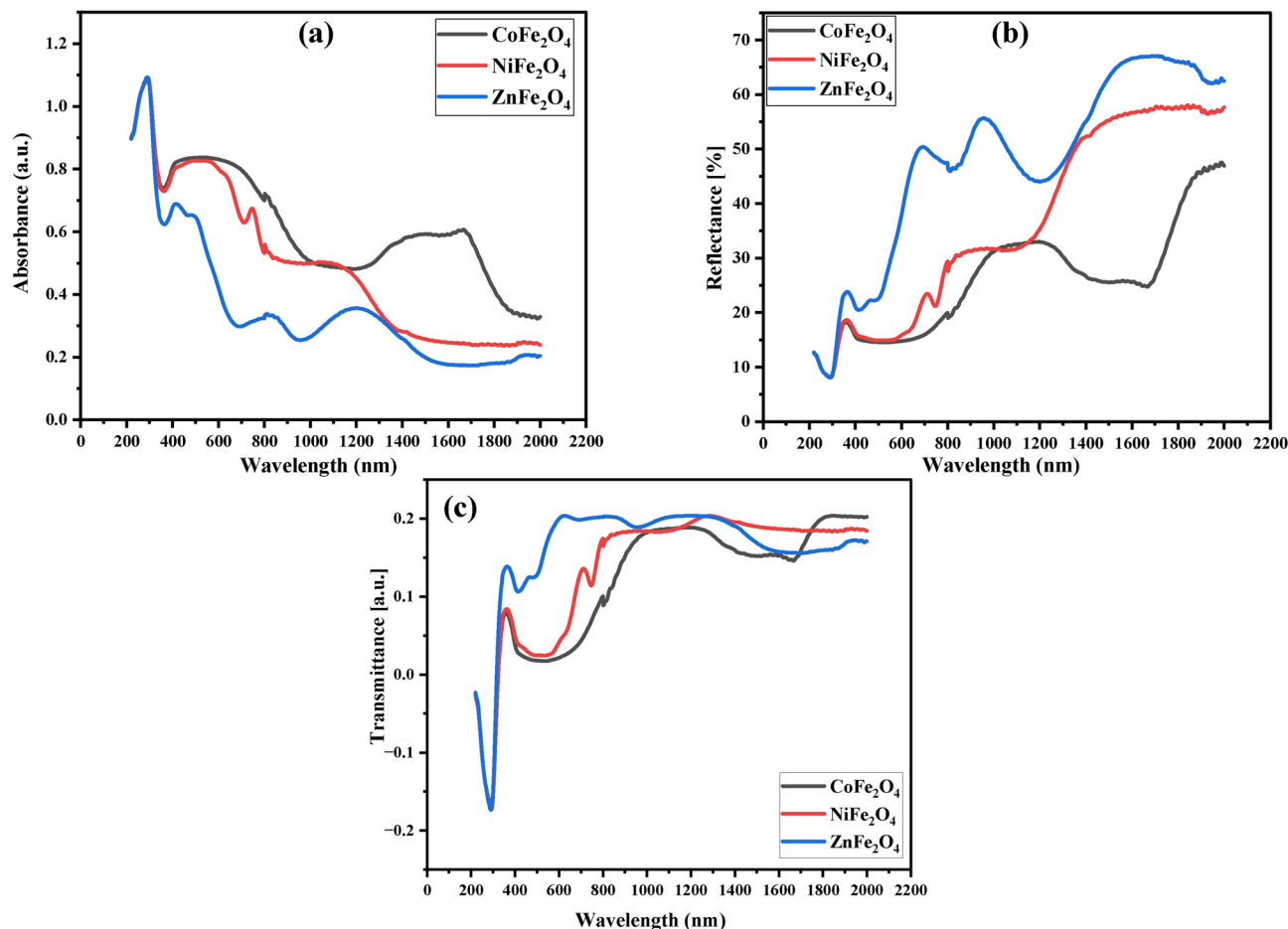
Fig. 6. Optical Absorption, Reflection, and Transmission Spectra. Absorption (**a**), reflection (**b**), and transmission (**c**) spectra for CoFe$_2$O$_4$, NiFe$_2$O$_4$, and ZnFe$_2$O$_4$ nanoparticles across UV, visible, and NIR regions. CoFe$_2$O$_4$ demonstrates maximum absorption, while ZnFe$_2$O$_4$ exhibits the highest reflection and transmission, supporting diverse optical applications.
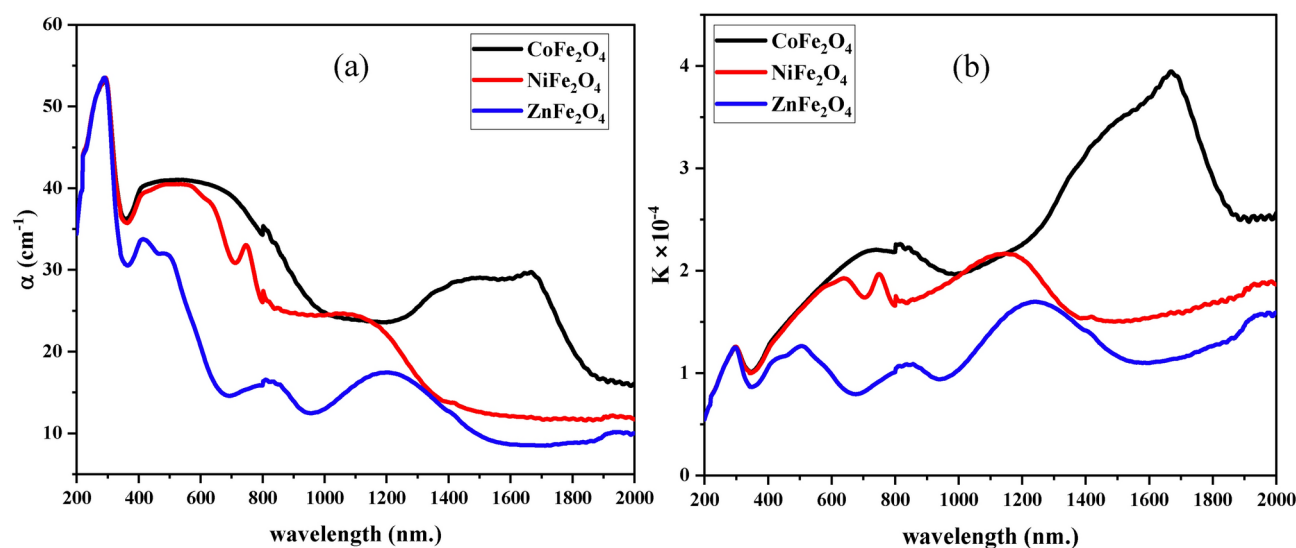

Fig. 7. Absorption and Extinction Coefficients. Graphs of absorption (**a**) and extinction coefficients (**b**) versus wavelength for CoFe$_2$O$_4$, NiFe$_2$O$_4$, and ZnFe$_2$O$_4$ nanoparticles. CoFe$_2$O$_4$ shows the highest absorption efficiency, highlighting its potential for light-blocking applications.

Compound	$Eg_{Dir.}$ (eV)	$Eg_{ind.}$ (eV)	Eu (eV)
$CoFe_2O_4$	3.3	1.9	0.14
$NiFe_2O_4$	3.5	2.1	0.30
$ZnFe_2O_4$	3.6	2.5	0.27

Table 5. direct band gap ($Eg_{dir.}$), the indirect band gap ($Eg_{ind.}$) and Urbach energy Eu of $CoFe_2O_4$, $NiFe_2O_4$ and $ZnFe_2O_4$.
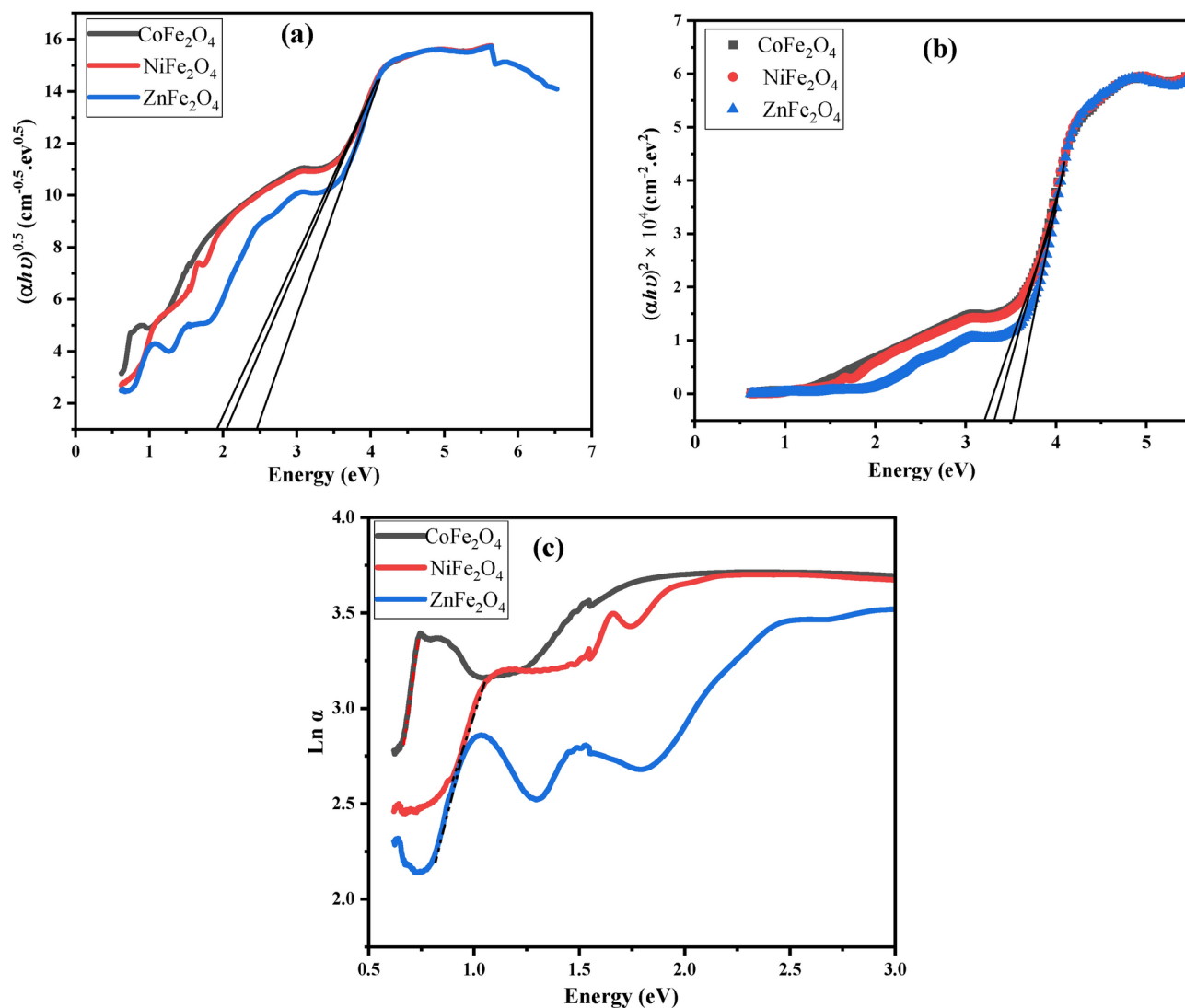
Fig. 8. Band Gap and Urbach Energy Analysis. Plots of $(\alpha h\nu)^{0.5}$ (**a**), $(\alpha h\nu)^2$ (**b**), and $Ln(\alpha)$ (**c**) as functions of photon energy for $CoFe_2O_4$, $NiFe_2O_4$, and $ZnFe_2O_4$. Results indicate direct and indirect band gap energies (3.3–3.6 eV) and structural disorder levels derived from Urbach energy values.

The Oxygen vacancies produced in the structure which disturb the system's band structure and increased the Urbach energy value which listed in Table 5.

The lowest Urbach energy was found in the $CoFe_2O_4$ sample indicating the lowest density of the structure disorder.

The values of α and extinction coefficient (K) are related to the interaction of the ferrites with the incident radiation. Depending on the wavelength and the material's energy gap Fig. 7(a, b), the absorption coefficient (α) and the extinction coefficient (K) can be calculated using the following formulas [79,81]:

$$\alpha = (2.303A)/l \qquad (7)$$

$$K = \frac{\alpha \lambda}{4\pi} \qquad (8)$$

Figure 7 (a, b) shows that absorption (α) and extinction coefficients (K) vary with wavelength. It is clear from the Figures that $CoFe_2O_4$ has the highest absorption efficiency, while $ZnFe_2O_4$ has the lowest absorption efficiency. This demonstrates the wide range of radiation absorption by ferrites, which is an important factor for their application in various fields.

The refractive index n, real and imajenary parts of dielectric constant ε_r and ε_i were determined for the investigated samples according to the following equations [82,83]:

$$n = \sqrt{\frac{4R}{(R-1)^2} - K^2} - \frac{(R+1)}{(R-1)} \qquad (9)$$

$$\varepsilon_r = n^2 - k^2, \qquad (10)$$

$$\varepsilon_i = 2nk \qquad (11)$$

where R is the reflectance.

The (Fig. 9 a–c) shows the decay of the refractive index n, ε_r, and ε_i with increasing the incident photon energy. At low energy values, the refractive index *n* was maximum due to the presence of the defect levels in the bandgap induced by the oxygen vacancies. These defect levels were responsible for an electronic transition between the valence band and the defect level, which is responsible for the high refractive index at low energy.
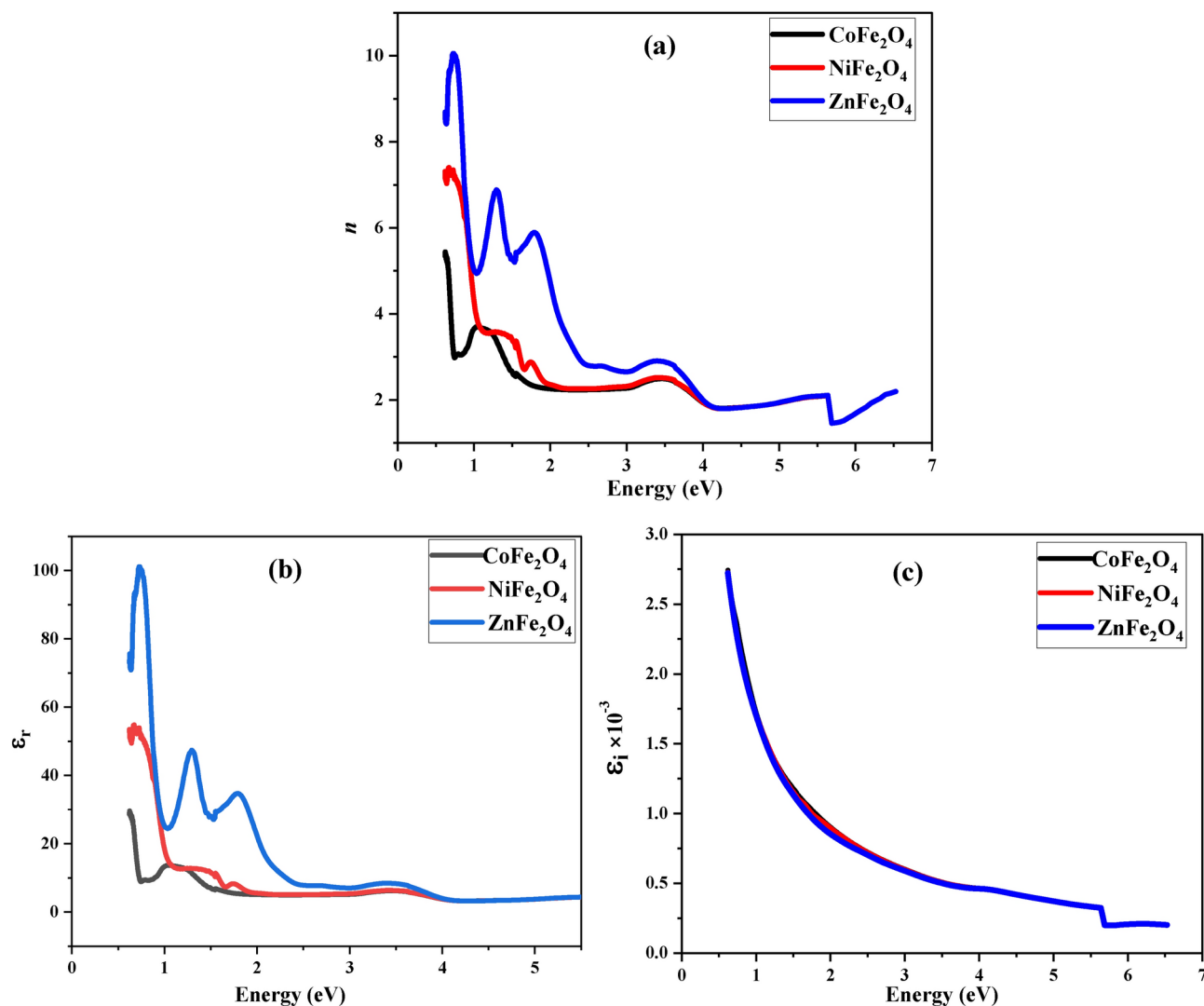
Fig. 9. Refractive Index and Dielectric Constants. Variation of refractive index (**a**), real dielectric constant (**b**), and imaginary dielectric constant (**c**) with photon energy for $CoFe_2O_4$, $NiFe_2O_4$, and $ZnFe_2O_4$. $CoFe_2O_4$ shows maximum refractive index values at low photon energy, attributed to oxygen vacancies.

Additionally, as the incident photon energy increased, the refractive index decreased due to the absence of the defect levels in the bandgap.

Furthermore, the electronic polarization of ions and local field in the optical material are associated to the refractive index. That's cusing the decreasing of ε_r and ε_i by increasing the incident photon energy shown in Fig. 9 (b, c).

The results of the optical conductivity σ_{opt} measurements show that the σ_{opt} increases with the incident photon energy, reaching a maximum at 4.3 eV. This increasing trend is attributed to the liberation of electrons from the valence band to the conduction band, which is caused by an absorption of the incident photon energy and a decrease in oxygen vacancies. This behavior is demonstrated in Fig. 10. The optical conductivity can be calculated using the following equation [84,85]:

$$\sigma_{opt.} = \frac{\alpha n c}{4\pi} \tag{12}$$

The results of this study suggest that $ZnFe_2O_4$ shows an impressive increase in non-linear refractive index (n^2) and third order of non-linear susceptibility $\chi^{(3)}$ in the range of short wave infrared radiation with a peak at 1692 nm. This increase is due to the decrease in mobile charges, which leads to a decrease in material polarization. Additionally, the linear optical susceptibility was also improved. These results Fig. 11 indicate that $ZnFe_2O_4$ is a promising material for non-linear optical $\chi^{(1)}$ applications [83]. The nonlinear parameters such as non-linear refractive index n_2, 3rd order non-linear optical susceptibility $\chi^{(3)}$. Also, the linear optical susceptibility $\chi^{(1)}$ was calculated using the following equations.

$$P = \chi^{(1)}E + P_{NL} \tag{13}$$

$$P_{NL} = \chi^{(2)}E^2 + \chi^{(3)}E^3 \tag{14}$$

$$\chi^{(1)} = \frac{(n^2 - 1)}{4\pi} \tag{15}$$

$$\chi^{(3)} = \frac{\xi}{(4\pi)^2}\left(n_o^2 - 1\right)^4 \tag{16}$$

where $\xi = 1.7 \times 10^{-10}$ (esu).

$$n_2 = \frac{12\pi\chi^{(3)}}{n_o} \tag{17}$$

Magnetic properties

Figure 12 illustrates the M-H magnetic loops of the AFe_2O_4 (A: Co, Ni and Zn) spinel ferrites at room temperature. The prepared samples $CoFe_2O_4$ and $NiFe_2O_4$ have ferrimagnetic behavior in the applied field range of -20,000 to 20,000 Oe, while $ZnFe_2O_4$ has antiferromagnetic behavior as shown in the inset of Fig. 12. The values of the saturation magnetization (M_s), the remanent magnetization (M_r), the coercivity (H_c) and the squareness ratio were reported in the Table 6. The magnetic properties of the ferrite materials depends on various parameters such as the morphology, crystallite size, magnetization direction.[34] It is noted that the magnetization ferrite
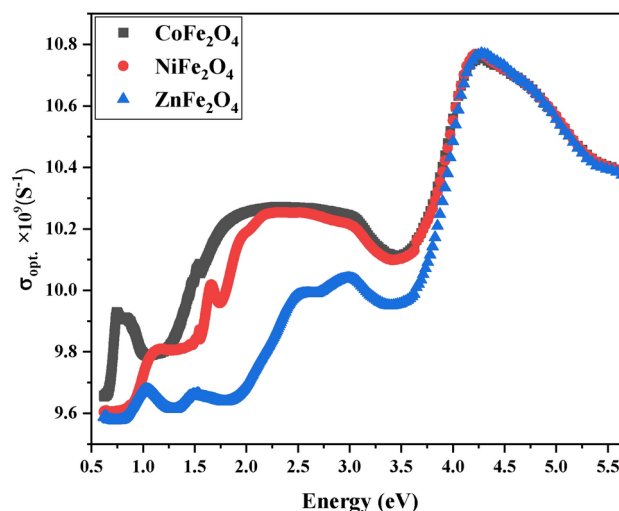
Fig. 10. Optical Conductivity. Graph of optical conductivity versus photon energy for $CoFe_2O_4$, $NiFe_2O_4$, and $ZnFe_2O_4$. $CoFe_2O_4$ exhibits the highest conductivity at 4.3 eV, corresponding to electron liberation from valence to conduction bands.
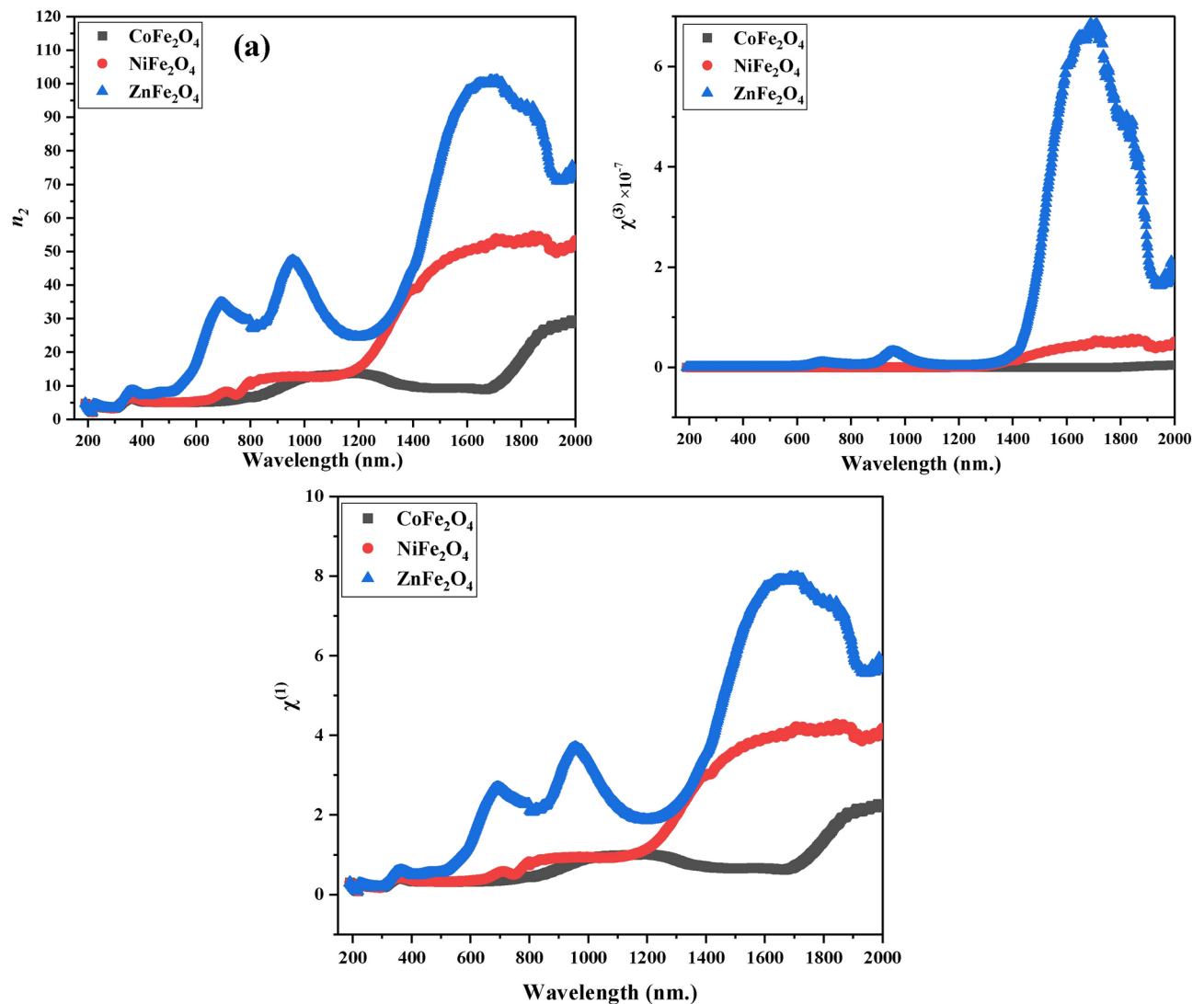
Fig. 11. Non-Linear Optical Properties. Plots of non-linear refractive index (**a**), third-order susceptibility (**b**), and linear optical susceptibility (**c**) for $CoFe_2O_4$, $NiFe_2O_4$, and $ZnFe_2O_4$. $ZnFe_2O_4$ displays a peak in short-wave infrared radiation, enhancing its suitability for optoelectronic applications.

AFe_2O_4 (A: Co, Ni and Zn) are strongly depend on the type of A cation. The highest value of M_s was observed for $CoFe_2O_4$ nanoparticles 55.97 emu/g while $ZnFe_2O_4$ has the lowest M_s which equals 0.025 emu/g because of the difference in the magnetic moment of A cation. The values of magnetic moment of Fe^{3+}, Co^{2+}, Ni^{2+} and Zn^{2+} are 5 μB, 3 μB, 2 μB and 0 μB, respectively [86]. The values of the coercive field are 1355 Oe, 137 Oe and 482 Oe for the nanoferrites $CoFe_2O_4$, $NiFe_2O_4$ and $ZnFe_2O_4$, respectively. The decrease of Hc of the $NiFe_2O_4$ and $ZnFe_2O_4$ than that of the $CoFe_2O_4$ related to the decrease in the anisotropy field and also the domain wall energy.

Magnetic interaction in the spinel ferrite (AB_2O_4) are originated from the three main magnetic interactions:

i. Intrasublattice magnetic interaction (A-A),
ii. Exchange magnetic interactions (B-B),
iii. super exchange magnetic interactions (A-B)

$CoFe_2O_4$ and $NiFe_2O_4$ are inverse spinel where the Co^{2+} and Ni^{2+} ions are placed in the octahedral B site while, Fe^{3+} ions are present in the tetrahedral A and octahedral B sites. Therefore, the magnetic interactions in the Co ferrite are $Fe_A^{3+} - Fe_B^{3+}$, $Fe_A^{3+} - Co_B^{2+}$, $Fe_A^{3+} - Fe_A^{3+}$, $Co_B^{2+} - Co_B^{2+}$, and $Fe_B^{3+} - Fe_B^{3+}$. While, the magnetic interactions in Ni ferrite are $Fe_A^{3+} - Fe_B^{3+}$, $Fe_A^{3+} - Ni_B^{2+}$, $Fe_A^{3+} - Fe_A^{3+}$, $Ni_B^{2+} - Ni_B^{2+}$, and $Fe_B^{3+} - Fe_B^{3+}$. The super-exchange magnetic interaction $Fe_A^{3+} - Fe_B^{3+}$ is main magnetic interaction and also is the stronger than the other and corresponding to the ferrimagnetic behavior for the samples $CoFe_2O_4$ and $NiFe_2O_4$. The M_s of the $CoFe_2O_4$ is greater than that of the $NiFe_2O_4$ owing to the magnetic moment of Co^{2+} ions is higher than that of Ni^{2+} ions. While, $ZnFe_2O_4$ is a normal spinel ferrite where Zn^{2+} ions are placed in the tetrahedral sites [A]. there is no magnetic interaction between A-A cations owing to the non magnetic
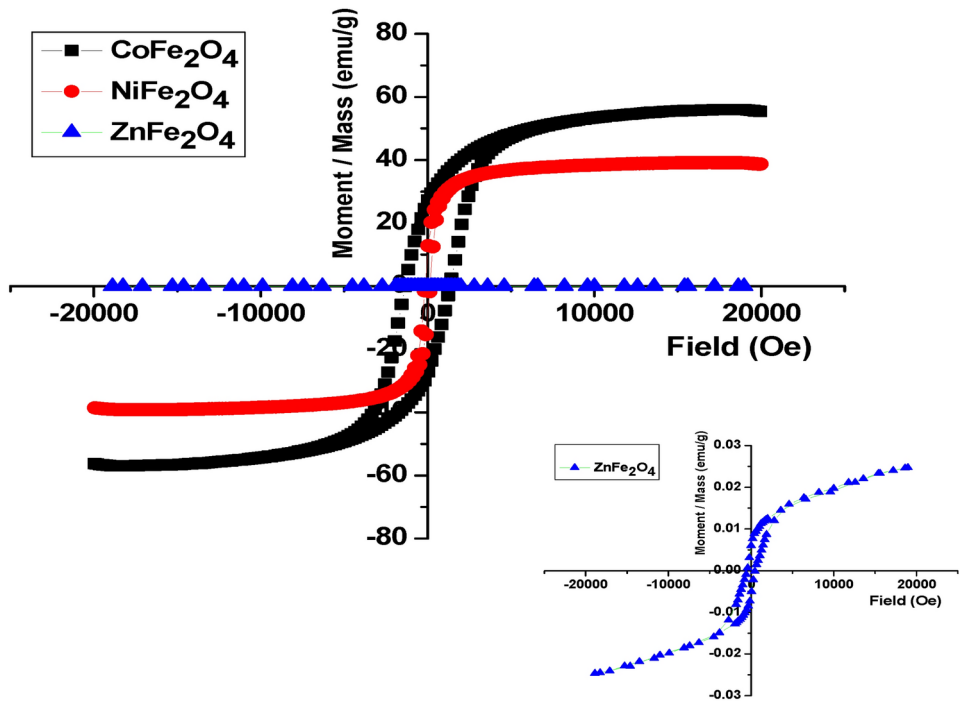
Fig. 12. Magnetic Hysteresis Loops. M-H magnetic loops of $CoFe_2O_4$, $NiFe_2O_4$, and $ZnFe_2O_4$ nanoparticles, showing ferrimagnetic behavior for $CoFe_2O_4$ and $NiFe_2O_4$, and antiferromagnetic properties for $ZnFe_2O_4$. Parameters include saturation magnetization, coercivity, and remanent magnetization, emphasizing diverse magnetic properties.

Samples	M_s (emu/g)	M_r (emu/g)	H_c (Oe)	SQR = M_r/M_s	K (erg/g)
$CoFe_2O_4$	56	27	1355	0.48	79,042
$NiFe_2O_4$	39	5	137	0.13	5595
$ZnFe_2O_4$	25×10^{-3}	6×10^{-3}	483	0.24	12.57

Table 6. The saturation magnetization (M_s), the remanent magnetization (M_r), the coercive field (H_c), and the anisotropy constant (K) for the investigated samples.

properties of Zn ions. The only magnetic interactions in $ZnFe_2O_4$ are originated between $Fe_{B}^{3+} - Fe_{B}^{3+}$ so the saturation magnetization of $ZnFe_2O_4$ is lower than $CoFe_2O_4$ and $NiFe_2O_4$. Also $Fe_B^{3+} - Fe_B^{3+}$ interaction is responsible for the antiferromagnetic properties of $ZnFe_2O_4$ ferrite. These results are compatible with the optical results where the exchange interaction responsible for the ferrimagnetic behavior can also influence the optical properties of the ferrite, particularly in the infrared region.

The anisotropy constant (K) value indicates a dipole's resistance to being destroyed by a reverse field and is strogly depends on thr coerceivity (H_c) and the saturation magnetization (M_s) according to the following equation[87]:

$$K = \frac{H_C \times M_S}{0.96} \qquad (18)$$

The values of K were reported in Table 6. The ratio between the M_r and M_s is define as the squareness ratio R which refres to the interaction between the magnetic domains. It has been reported that when R = 0.5, the coherent rotations occur in randomly oriented, non-interacting particles. While in the investigated nanosamples, the value of R < 0.5 which indicates that the magnetic particles are interacted magnetostatically [69].

Conclusion
Spinel ferrites of the form AFe_2O_4 (A: Co, Ni, Zn) were successfully synthesized and thoroughly characterized. Their optical and magnetic properties were systematically investigated.

- The prepared ferrites exhibit high transmittance in the visible, near-infrared (NIR), and short-wave infrared (SWIR) regions, making them suiTable for applications such as:Transparent electrodes in electronic devices

(e.g., touch screens, solar cells, displays). Optical and infrared filters for cameras and sensors. Optical waveguides and resonators.

- High nonlinear optical parameters ($\chi^{(3)} \approx 8$) were observed in the wavelength range of 1400–1900 nm, highlighting their potential for optoelectronic devices.
- The samples demonstrated excellent UV-blocking capabilities ($\alpha = 55$ cm^{-1} in the 200–300 nm range), making them ideal for UV detectors and photodiodes.
- Band gap energies ranged from 3.3 to 3.6 eV, influencing their absorption and reflection characteristics. Higher energy photons are absorbed, while lower energy photons are reflected.
- Refractive indices were found to increase at low energy values ($n \approx 10$ for energies < 1 eV), attributed to higher defect concentrations.
- Optical conductivity increased significantly with higher energy photons (up to 10×10^9 S^{-1} at 4.5 eV), indicating their efficiency for light-sensing applications.
- $CoFe_2O_4$ and $NiFe_2O_4$ exhibited ferrimagnetic behavior, while $ZnFe_2O_4$ displayed antiferromagnetic properties. These magnetic characteristics influence light-matter interactions, making them promising for advanced technological applications.

The combination of tunable optical and magnetic properties positions AFe_2O_4 spinel ferrites as versatile materials for a wide range of applications, including optoelectronics, photonics, and magnetic devices. Their unique properties make them an exciting area for further research and development.

Data availability
Derived data supporting the findings of this study are available from the corresponding author on request.

References
1. Hao, A. & Ning, X. Recent advances in spinel ferrite-based thin films: Synthesis, performances, applications, and beyond. *Front. Mater.* **8**, 719969 (2021).
2. Kefeni, K. K., Msagati, T. A. M., Nkambule, T. T. & Mamba, B. B. Spinel ferrite nanoparticles and nanocomposites for biomedical applications and their toxicity. *Mater. Sci. Eng. C.* **107**, 110314 (2020).
3. Qin, H. et al. Spinel Ferrites (MFe2O4): Synthesis, improvement and catalytic application in environment and energy field. *Adv. Colloid Interface Sci.* **294**, 102486 (2021).
4. Mathew, D. S. & Juang, R. S. An overview of the structure and magnetism of spinel ferrite nanoparticles and their synthesis in microemulsions. *Chem. Eng. J.* **129**, 51–65 (2007).
5. Kefeni, K. K. & Mamba, B. B. Photocatalytic application of spinel ferrite nanoparticles and nanocomposites in wastewater treatment: Review. *Sustain. Mater. Technol.* **23**, e00140 (2020).
6. Amiri, M., Salavati-Niasari, M. & Akbari, A. Magnetic nanocarriers: Evolution of spinel ferrites for medical applications. *Adv. Colloid Interface Sci.* **265**, 29–44 (2019).
7. Gaabour, L. H. Analysis of spectroscopic, optical and magnetic behaviour of pvdf/pmma blend embedded by magnetite (Fe₃O₄) nanoparticles. *Opt. Photon. J.* **10**, 197–209 (2020).
8. Alahmari, S. D. et al. Development of Mn doped CeTe as an environmental purifier for photodegradation of noxious methylene blue dye in water. *J. Phys. Chem. Solids* **188**, 111909 (2024).
9. Alanazi, M. M. et al. Synthesis of magnetic NiFe2O4/rGO heterostructure as potential photocatalyst for a breakdown of malachite green (MG) dye under the visible source of light. *Diam Relat Mater* **145**, 111128 (2024).
10. Alanazi, M. M. et al. Development of magnetically separable MoS2/NiFe2O4 heterostructure for improved photocatalytic efficiency of malachite green (MG) degradation. *J. Mater. Sci.: Mater. Electron.* **35**, 1045 (2024).
11. Alharbi, F. F. et al. Effect of Mn dopant on physiochemical properties of V2O5 and their photocatalytic application toward mineralization of malachite green (MG) dye. *Mater. Chem. Phys.* **322**, 129556 (2024).
12. Alharbi, F. F. et al. Development of Mn doped ZnAl2O4 via hydrothermal method as photocatalyst for Cr(VI) reduction under visible light. *Ceram. Int.* **50**, 24177 (2024).
13. Algarni, S. A. et al. Processing of Nb doped hematite for visible light photocatalytic reduction of noxious methylene blue. *Optik Stuttg* **287**, 171097 (2023).
14. Singh, S. & Khare, N. Low field magneto-tunable photocurrent in CoFe2O4 nanostructure films for enhanced photoelectrochemical properties. *Sci. Rep.* https://doi.org/10.1038/s41598-018-24947-2 (2018).
15. Illa, R. et al. Structural, magnetic, optical, and magneto-optical properties of CoFe2O4 thin films fabricated by a chemical approach. *Mater. Res. Bull.* **117**, 96–102 (2019).
16. Lu, Y. et al. Effect of Gd and Co contents on the microstructural, magneto-optical and electrical characteristics of cobalt ferrite (CoFe2O4) nanoparticles. *Ceram. Int.* **48**(2), 2782–2792 (2022).
17. Jeevanantham, B., Song, Y., Choe, H. & Shobana, M. K. Structural and optical characteristics of cobalt ferrite nanoparticles. *Mater. Lett. X* **12**, 100105 (2021).
18. Dinkar, D. K., Das, B., Gopalan, R. & Dehiya, B. S. Magnetic and optical properties of green synthesized nickel ferrite nanoparticles and its application into photocatalysis. *Nanotechnology* **32**, 505725 (2021).
19. Sundararajan, M. et al. A comparative study on NiFe2O4 and ZnFe2O4 spinel nanoparticles: Structural, surface chemistry, optical, morphology and magnetic studies. *Phys. B Condens. Matter.* **644**, 414232 (2022).
20. Jogi, J. K. et al. Investigation of the structural and optical properties of zinc ferrite nanoparticles synthesized via a green route. *J. Electron. Mater.* **51**, 5482–5491 (2022).
21. Kjeldby, S. B. et al. Optical properties of ZnFe2O4 nanoparticles and Fe-decorated inversion domain boundaries in ZnO. *Nanoscale Adv.* **5**, 2102–2110 (2023).
22. Dhanda, N., Thakur, P. & Thakur, A. Green synthesis of cobalt ferrite: A study of structural and optical properties. *Mater. Today Proc.* **73**, 237–240 (2023).
23. Ben Khalifa, S., Chebaane, S. & Beji, L. Optical and photoluminescence studies of CoFe2O4 nanoparticles deposited on different substrates. *Opt. Quant. Electron.* https://doi.org/10.1007/s11082-023-04737-5 (2023).
24. Aisida, S. O., Ahmad, I., Kai Zhao, T., Maaza, M. & Ezema, F. I. Calcination effect on the photoluminescence, optical, structural, and magnetic properties of polyvinyl alcohol doped ZnFe2O4 nanoparticles. *J. Macromol. Sci. Part B Phys.* **59**, 295–308 (2020).

25. Mishra, D. K. & Qi, X. Energy levels and photoluminescence properties of nickel-doped bismuth ferrite. *J. Alloys Compd.* **504**, 27–31 (2010).
26. Priyadharshini, P. & Pushpanathan, K. Synthesis of Ce-doped NiFe2O4 nanoparticles and their structural, optical, and magnetic properties. *Chem. Phys. Impact* **6**, 10021 (2023).
27. Singh, R. K. et al. Thermal, structural, magnetic and photoluminescence studies on cobalt ferrite nanoparticles obtained by citrate precursor method. *J. Therm. Anal. Calorim.* **110**, 573–580 (2012).
28. Ponpandian, N. et al. Néel temperature enhancement in nanostructured nickel zinc ferrite. *Appl. Phys. Lett.* https://doi.org/10.1063/1.1925755 (2005).
29. Raghavender, A. T., Zadro, K., Pajic, D., Skoko, Z. & Biliškov, N. Effect of grain size on the Néel temperature of nanocrystalline nickel ferrite. *Mater. Lett.* **64**, 1144–1146 (2010).
30. Chauhan, B. S., Kumar, R., Jadhav, K. M. & Singh, M. Magnetic study of substituted mg-mn ferrites synthesized by citrate precursor method. *J. Magn. Magn. Mater.* **283**, 71–81 (2004).
31. Hastings, J. M. & Corliss, L. M. Neutron diffraction studies of zinc ferrite and nickel ferrite. *Rev. Mod. Phys.* **25**, 114–119 (1953).
32. Stewart, S. J., Al-Omari, I. A., Sives, F. R. & Widatallah, H. M. Non-equilibrium cation influence on the Néel temperature in ZnFe2O4. *J. Alloys Compd.* **495**, 506–508 (2010).
33. Sodaee, T., Ghasemi, A., Paimozd, E., Paesano, A. & Morisako, A. The role of terbium cation substitution on the magnetic properties of cobalt ferrite nanoparticles. *J. Magn. Magn. Mater.* **330**, 169–173 (2013).
34. El-Masry, M. M., Mahmoud, A. E., Morshidy, H. Y. & Ramadan, R. Cu2+- and Zn2+-doped cobalt spinel ferrite: Insights on structural, thermal conduction, electric, magnetic and elastic properties. *J. Mater. Sci.: Mater. Electron.* **34**, 383 (2023).
35. Al Kiey, S. A., Ramadan, R. & El-Masry, M. M. Synthesis and characterization of mixed ternary transition metal ferrite nanoparticles comprising cobalt, copper and binary cobalt–copper for high-performance supercapacitor applications. *Appl. Phys. A* **128**, 473 (2022).
36. Shubhra, et al. Impact of doping Gd3+rare earth ion on structural, magnetic, and optical properties of cobalt and nickel ferrite nanomaterials. *Appl. Phys. A Mater. Sci. Process.* https://doi.org/10.1007/s00339-021-05011-9 (2021).
37. Slimani, Y. et al. Effect of bimetallic (Ca, Mg) substitution on magneto-optical properties of NiFe2O4 nanoparticles. *Ceram. Int.* **45**, 6021–6029 (2019).
38. Anh Tien, N. et al. Structural, optical and magnetic properties of Y-doped NiFe2O4 nanoparticles prepared by simple co-precipitation method. *Solid State Sci* **138**, 107149 (2023).
39. Wang, W. et al. Visible-light-activated TiO2–NiFe2O4 heterojunction for detecting sub-ppm trimethylamine. *J. Alloys Compd* **898**, 162990 (2022).
40. Xiao, N. et al. B, N-carbon dots-based ratiometric fluorescent and colorimetric dual-readout sensor for H2O2 and H2O2-involved metabolites detection using ZnFe2O4 magnetic microspheres as peroxidase mimics. *Sens. Act. B Chem* **273**, 1735–1743 (2018).
41. Natarajan, K., Singh, P., Bajaj, H. C. & Tayade, R. J. Facile synthesis of TiO2/ZnFe2O4 nanocomposite by sol-gel auto combustion method for superior visible light photocatalytic efficiency. *Korean J. Chem. Eng.* **33**, 1788–1798 (2016).
42. Yadav, N. G. et al. Impact of collected sunlight on ZnFe2O4 nanoparticles for photocatalytic application. *J. Colloid Interface Sci.* **527**, 289–297 (2018).
43. Sahoo, R. et al. Hierarchical growth of ZnFe2O4 for sensing applications. *New J. Chem.* **40**, 1861–1871 (2016).
44. Layek, S. & Verma, H. C. Magnetic and dielectric properties of multiferroic BiFeO3 nanoparticles synthesized by a novel citrate combustion method. *Adv. Mater. Lett.* **3**, 533–538 (2012).
45. Imtiaz, M. et al. Designing and tailoring of photocatalytic properties of NiMnO3 by using the doping strategy. *Optik Stuttg* **300**, 171639 (2024).
46. Seliem, A. F. et al. Development of Nb-Doped BiFeO3 via hydrothermal method for photocatalytic degradation of rhodamine B (RhB) Dye. *JOM* **76**, 408–417 (2024).
47. Arman, M. M. & El-Masry, M. M. Novel NdFeO$_3$/PVDF and M-doped NdFeO$_3$/PVDF (M = Ni, Zn) nanocomposites for energy storage and flexible electronics. *Ceram. Int.* **51**, 7178 (2025).
48. Alsalhi, S. A. et al. Development of a CeTe/rGO nanosized composite for photoreduction of heavy metal in the aquatic environment. *J. Electron. Mater.* **53**, 4553–4563 (2024).
49. Abdullah, M. et al. Facile synthesis of MnO2/g-C3N4 for photocatalytic reduction of methylene blue dye under visible light. *J. Mater. Sci. Mater. Electron.* https://doi.org/10.1007/s10854-024-12166-7 (2024).
50. Ateia, E. E., Gawad, D. & Arman, M. M. Ab-initio study of structural, morphological and optical properties of multiferroic La2FeCrO6. *J. Alloys Compd* **976**, 173017 (2024).
51. Ateia, E. E., Reda, M., El-Dek, S. I. & Arman, M. M. A comparative approach for estimating microstructural characteristics of BaTi1−xZrxO3 (0.0 ≤ x ≤ 0.3) nanoparticles via X-ray diffraction patterns. *J. Solgel. Sci. Technol.* **110**, 887 (2024).
52. Abdel-karim, A. M., Ahmed, Y. M. & El-Masry, M. M. Ag-CuO/epoxy hybrid nanocomposites as anti-corrosive coating and self-cleaning on copper substrate. *Sci. Rep.* **13**, 19248 (2023).
53. El-Masry, M. M. & Dek, S. I. E. Enhanced dielectric permittivity of novel ternary La2Cu–AgO4 nanocomposites with different ratios of 2-D Borophene nanofiller. *Ceram. Int.* **49**(21), 33628–33642 (2023).
54. El-Masry, M. M. Synthesize and characterization of Ag-CuO/rGO nanoparticles as a filler of the PVDF polymer to improve its polar β phase and electrical conductivity for polymer batteries applications. *J. Polym. Res.* https://doi.org/10.1007/s10965-023-03727-1 (2023).
55. Vazquez-Olmos, A. R. et al. Mechanosynthesis of MFe2O4 (M = Co, Ni, and Zn) Magnetic nanoparticles for Pb removal from aqueous solution. *J. Nanomater.* **2016**, 1–9 (2016).
56. Zhang, M. et al. Catalytic activity of ferrates (NiFe2O4, ZnFe2O4 and CoFe2O4) on the thermal decomposition of ammonium perchlorate. *Propellants, Explos., Pyrotech.* **45**, 463–471 (2020).
57. Iftikhar, S. et al. The impact of carbon nanotubes on the optical, electrical, and magnetic parameters of Ni2+ and Co2+ based spinel ferrites. *Ceram. Int.* **45**(17), 21150–21161 (2019).
58. Ati, A. A. Fast synthesis, structural, morphology with enhanced magnetic properties of cobalt doped nickel ferrite nanoscale. *J. Mater. Sci. Mater. Electron.* **29**(14), 12010–12021 (2018).
59. Saleem, A. et al. Facile hydrothermal synthesis of visible-light-driven MnS/rGO nanocomposite for photocatalytic degradation of methylene blue dye. *Phys. Status Solidi a* **220**, 2200734 (2023).
60. Alburaih, H. A. et al. Synergistic photodegradation of methylene blue by Sm doped Fe2O3 photocatalyst under sunlight. *Chin. J. Phys.* **83**, 637–649 (2023).
61. Abudllah, M. et al. Facile fabrication of ternary CuO/CuS/ZnS for photodegradation of methylene blue. *J. Korean Ceram. Soc.* **60**, 569–580 (2023).
62. Tamam, N. et al. Surfactant assisted synthesis of nanostructured Mn-doped CuO: An efficient photocatalyst for environmental remediation. *Ceram. Int* **48**, 29589–29600 (2022).
63. Alharbi, F. F. et al. Correction to: CuO/ZnTe nanocomposite for photodegradation of malachite green from industrial effluents to clean environment. *J. Mater. Sci. Mater. Electron.* **34**, 2150 (2023).
64. Alharbi, F. F. et al. CuO/ZnTe nanocomposite for photodegradation of malachite green from industrial effluents to clean environment. *J. Mater. Sci. Mater. Electron.* **34**, 2150 (2023).
65. Alharbi, F. F. et al. CuO/ZnTe nanocomposite for photodegradation of malachite green from industrial effluents to clean environment. *J. Mater. Sci. Mater. Electron.* https://doi.org/10.1007/s10854-023-11600-6 (2023).

66. Khan, K. et al. Structural, electrical, and photocatalytic properties of Y-type hexaferrite/carbon dot composite. *J. Mater. Sci. Mater. Electron.* https://doi.org/10.1007/s10854-023-11143-w (2023).

67. Alharbi, F. F. et al. Investigation of photoreduction of Cr (VI) and electrocatalytic properties of hydrothermally produced novel CoFe2O4/ZnO nanostructure. *Solid State Sci.* **143**, 107278 (2023).

68. Alenad, A. M. et al. Visible light driven Ni doped hematite for photocatalytic reduction of noxious methylene blue. *Mater. Res. Bull.* **165**, 112306 (2023).

69. Arman, M. M. & El-Dek, S. I. Structural, surface, magnetic study and application of nanoparticles CoFe2O4 ZnO and its Nanocomposite. *J. Supercond. Nov. Magn.* **36**, 1913–1925 (2023).

70. El-Masry, M. M., El-Shahat, M., Ramadan, R. & Abdelhameed, R. M. Selective photocatalytic reduction of nitroarenes into amines based on cobalt/copper ferrite and cobalt-doped copper ferrite nano-photocatalyst. *J. Mater. Sci.: Mater. Electron.* **32**, 18408 (2021).

71. Rafiq, M. A., Javed, A., Rasul, M. N., Khan, M. A. & Hussain, A. Understanding the structural, electronic, magnetic and optical properties of spinel MFe2O4 (M = Mn Co, Ni) ferrites. *Ceram. Int.* **46**, 4976–4983 (2020).

72. Joshi, S. et al. Structural, magnetic, dielectric and optical properties of nickel ferrite nanoparticles synthesized by co-precipitation method. *J. Mol. Struct.* **1076**, 55–62 (2014).

73. Khan, A. A. et al. Influence of preparation method on structural, optical and magnetic properties of nickel ferrite nanoparticles. *Mater. Sci. Poland* **35**, 58–65 (2017).

74. Tatarchuk, T. R. et al. Effect of cobalt substitution on structural, elastic, magnetic and optical properties of zinc ferrite nanoparticles. *J. Alloys Compd.* **731**, 1256 (2018).

75. Gharibshahi, E., Young, B. D., Bhalla, A. S. & Guo, R. Theory, simulation and experiment of optical properties of cobalt ferrite (CoFe2O4) nanoparticles. *J. Mater. Sci. Technol.* **57**, 180–187 (2020).

76. Khairy, M. & Gouda, M. E. Electrical and optical properties of nickel ferrite/polyaniline nanocomposite. *J. Adv. Res.* **6**, 555–562 (2015).

77. Singh, P. et al. In situ high temperature XRD studies of ZnO nanopowder prepared via cost effective ultrasonic mist chemical vapour deposition. *Bull. Mater. Sci.* **31**, 573–577 (2008).

78. N. N. Jandow, N. F. Habubi, S. S. Chiad, I. A. Al-Baidhany, and M. A. Qaeed, Annealing effects on band tail width, urbach energy and optical parameters of Fe2O3:Ni thin films prepared by chemical spray pyrolysis technique, International Journal of Nanoelectronics and Materials **12**, (2019).

79. Davis, E. A. & Mott, N. F. Conduction in non-crystalline systems V Conductivity, optical absorption and photoconductivity in amorphous semiconductors. *Philos. Mag.* **22**, 0903–0922 (1970).

80. M. M. El-Masry, A. M. Abd ELwahab, and M. M. Arman, Nanoparticles-Based Optical Chemosensors for Lead Acetate Sensing in Water: ZnO, Zn0.97Ce0.03O, and Zn0.97Nd0.03O, J Fluoresc (2025).

81. Srinet, R., Nandy, S. & Patel, N. R. Estimating leaf area index and light extinction coefficient using Random Forest regression algorithm in a tropical moist deciduous forest India. *Ecol. Inform.* **52**, 94–102 (2019).

82. Aftab, M., Butt, M. Z., Ali, D., Bashir, F. & Khan, T. M. Optical and electrical properties of NiO and Cu-doped NiO thin films synthesized by spray pyrolysis. *Opt Mater (Amst)* **119**, 111369 (2021).

83. El-Masry, M. M. & Ibrahim, A. S. Ag-CuO/rGO/PVDF nanocomposite synthesized via simple method as a broadband non-linear optical material for optronic applications. *J. Mater. Sci. Mater. Electron.* **33**, 10851–10865 (2022).

84. El-Masry, M. M. & Ramadan, R. Enhancing the properties of PVDF/MFe2O4; (M: Co–Zn and Cu–Zn) nanocomposite for the piezoelectric optronic applications. *J. Mater. Sci. Mater. Electron.* **33**, 15946 (2022).

85. El-Masry, M. M. & Ramadan, R. The effect of CoFe2O4, CuFe2O4 and Cu/CoFe2O4 nanoparticles on the optical properties and piezoelectric response of the PVDF polymer. *Appl. Phys. A Mater. Sci. Process.* https://doi.org/10.1007/s00339-021-05238-6 (2022).

86. Arman, M. M. The effect of the rare earth A-site cation on the structure, morphology, physical properties, and application of perovskite AFeO3. *Mater. Chem. Phys.* **304**, 12782 (2023).

87. M. M. Arman, Effect of divalent cations (Co2+ and Ni2+) on microstructure, physical properties and application of Nd, Journal of Rare Earths (2023).

Author contributions

Mai M. El-Masry: Conceptualization, Methodology, Formal analysis, Data curation, Investigation, Writing, review. M.M. Arman:,Conceptualization, Methodology, Formal analysis, Data curation, Investigation, Writing, review.

Funding

Declarations

Competing interests

The authors declare no competing interests.

Ethical approval

We consciously assure that for the manuscript Emerging Applications: AFe2O4 Spinel Ferrites; (A: Co, Ni and Zn) with High Transmittance and UV Blocking Properties. The following is fulfilled: (1) This material is the author's own original work, which has not been previously published elsewhere. (2) The paper is not currently being considered for publication elsewhere. (3) The paper reflects the authors' own research and analysis in a truthful and complete manner. (4) The paper properly credits the meaningful contributions of co-authors and co-researchers. (5) The results are appropriately placed in prior and existing research. (6) All sources used are properly disclosed (correct citation). Literally copying of text must be shown as such by using quotation marks and giving proper reference. (7) We have been personally and actively involved in substantial work leading to the paper and will take public responsibility for its content.

Additional information

Correspondence and requests for materials should be addressed to M.M.E.-M.

Reprints and permissions information is available at www.nature.com/reprints.